scientific reports

Check for updates

OPEN

Light-induced negative differential resistance and neural oscillations in neuromorphic photonic semiconductor micropillar sensory neurons

Bejoys Jacob[1]✉, Juan Silva[1], José M. L. Figueiredo[2], Jana B. Nieder[1] & Bruno Romeira[1]✉

Neuromorphic systems, inspired by nature, are sought to efficiently process analogue inputs in real and complex environments. This could lead to ultralow-power in-sensor intelligent edge computers. Here, we present an artificial sensory oscillator neuron consisting of a III–V semiconductor micropillar quantum resonant tunnelling diode (RTD) with GaAs photosensitive absorption layers. The oscillatory optical neuron encodes incoming analogue optical data into spatiotemporal oscillatory signals. We demonstrate that near-infrared light within a certain intensity range activates a region of negative differential resistance, and subsequently, large-amplitude voltage oscillations. As a result, optic analogue information is encoded into electrical oscillations resulting in amplification of sensory light inputs. Under pulse-modulated light, excitation and inhibition of burst firing patterns can be controlled within a single oscillatory neuron, simulating neural activity in networks in the form of breather-type oscillatory phenomena. Such spatiotemporal oscillatory patterns (burst firing) form the basis for the combined sensing, pre-processing, and encoding abilities of the vision-nervous system found in biological organisms. This work paves the way for future artificial visual systems using III–V semiconductor nano-optoelectronic circuits in applications for light-driven neurorobotics, bioinspired optoelectronics, and in-sensor neuromorphic computing systems for real-time processing of sensory data.

Neurons are the fundamental building blocks of the nervous system and are used to transmit and process electrochemical signals. They operate in a liquid electrolyte and communicate with each other via synapses which control the gradual and activity-dependent coupling between the axon of pre-synaptic neurons and the dendrite of post-synaptic neurons. Neuromorphic computing emulates synapses and neurons using hardware for efficient brain-inspired computation[1]. Synapses are typically emulated using memory devices[2] (e.g. non-volatile) which can be binary, multistate or analogue. However, to emulate the physiology of neurons, and their oscillatory dynamics[3], additional electronic[4,5], and/or optoelectronic[6] circuitry is required at the expense of increasing power consumption and footprint. The development of miniaturized hardware that replicates such spatiotemporal dynamics is essential since oscillatory phenomena plays a crucial role in neuronal activity[3], and can be readily observed in local field potential and electroencephalogram signals[7]. In insects, the rhythmic burst firing in clock neurons sustains circadian timekeeping of locomotor rhythms in drosophila brain[8], and in the dragonfly visual system neurons respond to moving targets with a series of spike bursts enhancing the robustness of target-evoked responses[9]. In the mammalian brain, oscillatory dynamics governs propagating neuronal activity in cortical-hippocampal circuits[10], and provides amplification of sensory inputs[11]. Also, respiration-locked neuronal oscillations in the olfactory bulb have been found to control delta band neuronal oscillations in the somatosensory cortex of mice[12], revealing the importance of oscillatory phenomena in biological organisms.

A considerable amount of neuromorphic devices have been shown recently aiming at realizing bioinspired nonlinear sensory neuronal responses to build a new class of intelligent sensory systems[13–19]. They include stochastic phase-change neurons[20], bioinspired organic artificial afferent nerves[21], and artificial nociceptors based on diffusive memristors[22]. These systems are responsive to electrical or other physical signals such as pressure

[1]INL—International Iberian Nanotechnology Laboratory, Av. Mestre José Veiga S/N, 4715-330 Braga, Portugal. [2]LIP - Laboratório de Instrumentação e Física Experimental de Partículas, Departamento de Física, Faculdade de Ciências, Universidade de Lisboa, 1749-016 Lisboa, Portugal. ✉email: bejoys.jacob@inl.int; bruno.romeira@inl.int

or temperature. More recently, efforts have been made towards neuromorphic components that are responsive to optical stimuli to process visual information. These include artificial optic-neural synapses for color-mixed pattern recognition using h-BN/WSe_2 heterostructures[23], artificial sensory neurons consisting of $InGaZnO_4$-based optical sensors, and NbO_x-based oscillator neurons[24]. Instead of adopting new materials with inherent challenges, for future scalable network systems, III–V compound semiconductors (e.g., InP or GaAs) have been proposed as neuromorphic light-sensitive and emitting devices[25], an approach already well-matched with mature optoelectronic devices (e.g. LEDs, lasers and photodiodes). Notable examples include excitable neuron using a distributed feedback laser with a saturable absorber[26], vertical-cavity surface-emitting laser (VCSEL) sources as artificial spiking neurons[27], among other approaches (review in[28]). Recently, III–V photosensitive and emitting nanowires have been proposed for insect brain computational circuits[29], and quantum resonant tunnelling diode photodetectors (RTD-PDs) to enable voltage-controlled negative differential resistance (NDR)[30], which emulates the FitzHugh–Nagumo neuron model[31]. The intrinsic electrical gain effect from the voltage-controlled NDR has been extensively studied to provide excitable spiking and other dynamic neural phenomena[32,33]. Taking advantage of the NDR effect and photosensitivity of III–V RTD-PDs, optically-triggered excitable spiking has been achieved[34]. However, miniaturized photonic devices with seamless integration of both sensory and oscillatory neurons remains unexplored. Since biophysical studies reveal that even single neurons are capable of complex oscillatory dynamics[35], such as resonate at multiple frequencies, emulating oscillatory phenomena in compact optoelectronic neuron circuits is highly relevant for new applications in neuromorphic optical computing systems.

In this work, we present a III–V neuromorphic photonic micropillar RTD photodetector (μRTD-PD). The μRTD-PD emulates sensory oscillatory neurons capable of processing optical information. We demonstrate that near-infrared continuous-wave (CW) light, within a certain intensity range, induces a region of NDR, enabling voltage- and optically-controlled NDR. Subsequently, optic analogue information is encoded into spatiotemporal large-amplitude electrical oscillations resulting in amplification of sensory inputs. We demonstrate that a single oscillatory neuron under pulse-modulated light provides excitation and inhibition of burst firing patterns. The stability and temporal response of the spatiotemporal burst firing patterns are analysed in the context of breather-type oscillations which represent emulation of neural activity in networks. Such spatiotemporal oscillatory patterns (burst firing) form the basis for the combined sensing, pre-processing, and encoding abilities within the same neuromorphic device, while previous demonstrations of multi-functions require multi-integrated optoelectronic components, thus increasing the complexity, cost and size of the neuromorphic system. The neuromorphic photonic sensory oscillator neuron demonstrated here paves the way to miniaturized biological-inspired processors of visual information. The approach is already compatible with proven III–V semiconductor platforms which have matured to meet the demanding industrial requirements in 3D sensing and light detection and ranging (LiDAR), thus uniquely suited to operate over a wide-range of wavelengths and optoelectronic applications.

Results

Device design and fabrication

The biological sensory oscillator neuron and its optical semiconductor counterpart are displayed in Fig. 1. In Fig. 1a is shown an illustration of a visual (eye) and processing (neuron) biological system converting light signals into neuronal oscillatory electrical responses to process visual information. This behaviour is emulated by the μRTD-PD sensory oscillator neuron device shown in Fig. 1b, and its equivalent lumped electric circuit is displayed in Fig. 1c. The active element of the μRTD-PD sensory neuron consists of a III–V *n*-type micropillar RTD with photosensitive layers and double barrier quantum well (DBQW) layers, Fig. 1b. In the inset of the micropillar μRTD-PD (left hand side) is shown the energy band diagram (at zero voltage) depicting the AlAs/GaAs/AlAs (~ 10 nm wide) DBQW region (the epilayer stack of the entire device is described in Methods). Under an applied forward bias (current flowing from top contact to bottom contact) the resonant energy levels in the GaAs quantum well are swept through the emitter Fermi sea, resulting in an N-shape current–voltage (I–V) characteristic with a local current maximum (referred as peak) and a minimum (referred as valley). Since the device is unipolar (*n*-type), an anti-symmetric I–V is also expected under reverse bias conditions. In both forward and reverse applied voltage scenarios, the DBQW acts as an electron energy filter controlling the current flow via quantum resonant tunnelling, where the maximum and minimum current flow corresponds to the highest and lowest probability, respectively, of charge carriers tunnelling through the quasi-bounded states of the DBQW. The lumped circuit of the photosensitive μRTD-PD (purple dashed region) is shown in Fig. 1c (see circuit model in Supplementary). For voltage and light conditions where negative resistance exists, Fig. 1d, the electrical gain provided by the NDR effect, together with the resonant tank *LC* circuit, enables self-sustaining oscillations among other rich dynamic phenomena[36].

The NDR region is key to achieve self-sustained oscillations in our photosensitive neuron. The NDR is quantified by the peak to valley current ratio (PVCR = I_p/I_v) and by the ratio $\Delta V/\Delta I$, where $\Delta V = V_v\text{-}V_p$ is the difference in valley voltage, V_v, and peak voltage, V_p, and $\Delta I = I_p - I_v$ is difference between peak current, I_p, and valley current, I_v. In the DBQW AlAs/GaAs/AlAs material system studied here the PVCR is typically much lower, $(I_p/I_v) < 5$, than in other materials systems, such as in the DBQW AlAs/InGaAs/AlAs, $(I_p/I_v) > 10$[37]. The low PVCR (or absence of PVCR) at room-temperature for the AlAs/GaAs/AlAs system is due to the lower energy difference of the DBQW AlAs/GaAs/AlAs and the larger electron effective mass when compared to other heterostructures.

As discussed in the next sections, for the III–V epilayer stack shown in Fig. 1b only positive differential regions (PDR) have been measured under dark conditions (black dashed line of Fig. 1d). However, when the μRTD-PD is illuminated, (purple solid trace in Fig. 1d), pronounced NDR effect can be achieved enabling voltage- and light-control of the NDR effect in our neuron devices. The light-induced effect is related to the

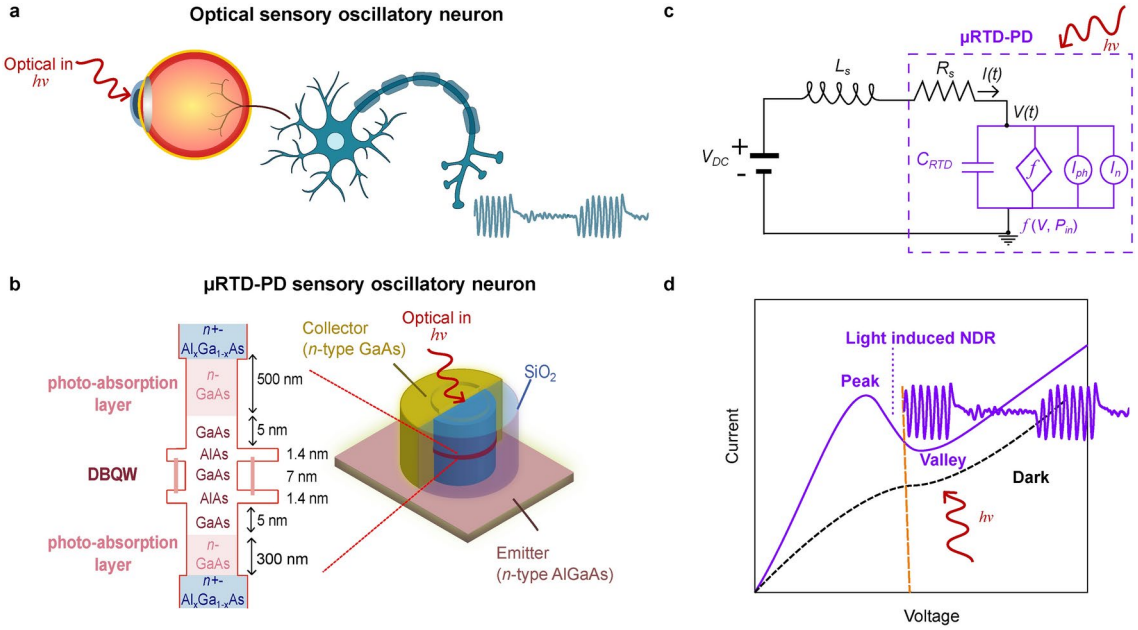

Fig. 1. Optical sensory oscillatory neuron concept. (**a**) Schematic showing a biological optical sensory oscillatory neuron system found in the visual system that senses and converts optical signals into electrical oscillations. (**b**) The μRTD-PD sensory oscillator neuron device mimicking the biological system. In the inset is displayed the energy band diagram of the semiconductor stacked epilayers forming the micropillar showing the dimensions of the intrinsic double barrier quantum well (DBQW) region and the surrounding collector and emitter *n*-type GaAs light absorption layers. (**c**) Lumped electrical circuit of the μRTD-PD sensory oscillator neuron device, where L_s is the μRTD-PD connecting circuitry equivalent inductance, R_s accounts for the μRTD-PD series resistance and remaining circuitry resistance, C_{RTD} is the equivalent device's and circuitry capacitance, and $f(V, P_{in})$ is the light and voltage controlled current source that mimics the RTD current-voltage (I–V) characteristic (which depends on the bias voltage and incident light intensity), I_{ph} is the photocurrent, and I_n is the associated noise of the system. (**d**) I–V characteristic exemplifying the operation of the μRTD-PD oscillatory neuron under dark and illumination conditions. Under dark conditions (black dashed trace) only positive differential resistance regions (PDR) are present. Under illumination conditions (purple solid line), an N-shaped I–V with 'peak', 'valley' and negative differential resistance (NDR) region is obtained.

dynamics of electron-hole pair generation and charge accumulation in the DBQW and the surrounding regions. In this work, the NDR effect is controlled by the light intensity and modulation conditions, which is explored to switch on and off self-sustained oscillations and operate these devices as sensory oscillator neurons.

To study the optical sensing and oscillatory phenomena, *n*-type μRTD-PD devices were fabricated in shape of micropillars with diameter, *d*, ranging from 6 to 10 μm, with both top (collector) and bottom (emitter) contacts (assuming forward bias). Scanning electron microscope (SEM) images of fabricated μRTD-PDs with diameters of 6 μm, 8 μm, and 10 μm are shown in Fig. 2. A dielectric material, SiO_2, protects and electrically isolates the micropillar structures. Further, when combined with chemical pre-treatment using sulphide ammonia[38], the SiO_2 provides a surface passivating material. To enable light receiving operation, a half-circle metal layer contact was covering the top part of each micropillar, while keeping the other half uncovered for illumination purposes. Details on the fabrication of electrically-connected GaAs-based micropillar devices can be found in the methods section and in[39].

Light-activation of negative differential resistance

The static I-V characteristics of fabricated μRTD-PD sensory neuron devices were investigated under dark and light conditions. The CW illumination at $\lambda \sim 830$ nm wavelength was provided by a laser diode through a single-mode fibre, and the light was coupled to the top micropillar using a lensed fibre (see details in Methods). In Fig. 3 is shown the schematic of the characterization setup used to obtain the static and dynamic (next section) photoresponse.

In Fig. 4a the dark and illuminated I–Vs are shown under forward and reverse bias conditions for micropillar devices ranging from 6 to 10 μm. Under forward bias, the dark I–Vs (dashed traces in Fig. 4a) show positive differential resistance, without signatures of NDR. Under reverse bias voltage, nonlinear regions can be observed around $V_{DC} = -3$ V, showing evidence of signatures of NDR. When illuminated, P_{in}, of ~ 3.7 mW and $\lambda \sim 830$ nm, a pronounced increase of the photocurrent is observed in the so-called peak voltage, solid traces in Fig. 4a. This is attributed to the increase of electron density in the 500 nm GaAs light sensitive layer. This leads to a built-in electric field modulation caused by photogenerated charge accumulation in the regions surrounding the

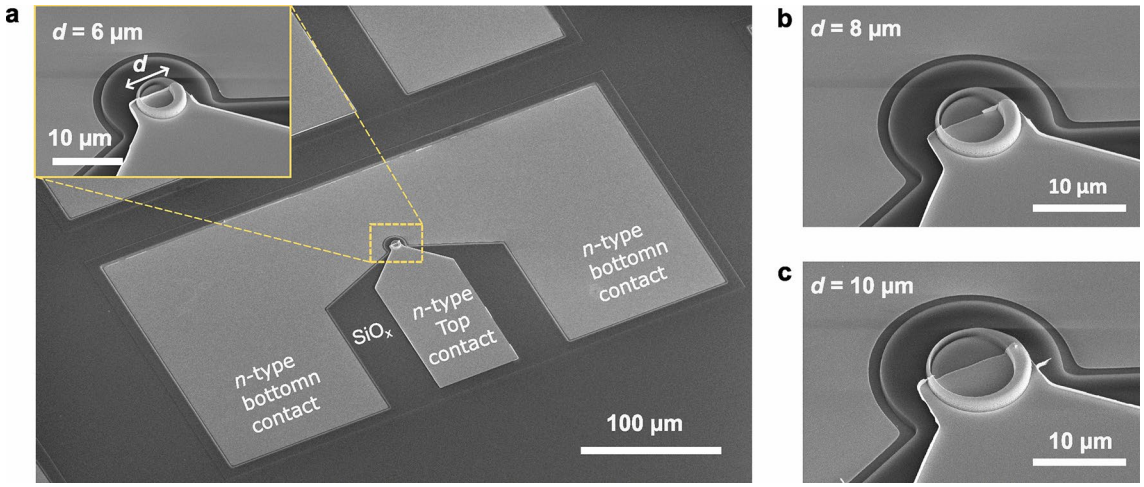

Fig. 2. Scanning electron microscope (SEM) images of fabricated µRTD-PD sensory oscillator neuron devices with increasing micropillar diameters (d). (**a**) Overview of an entire device with $d = 6$ µm. Inset is displayed a magnified image of the micropillar region. Magnified images of micropillars of devices with diameters of (**b**) $d = 8$ µm, and (**c**) $d = 10$ µm.

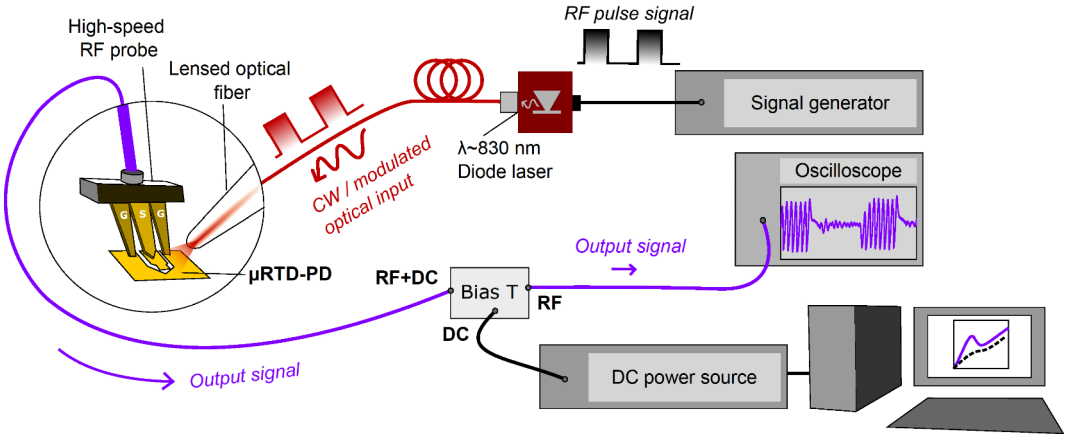

Fig. 3. Schematic of the static and dynamic photoresponse characterization setup of the µRTD-PD. The device is electrically probed and illuminated using a continuous wave (CW) diode laser ($\lambda \sim 830$ nm) coupled to an optical fibre. The current–voltage (I–V) static characteristic of dark and illuminated devices is measured in the DC port of the bias-T. For characterization of the dynamic response, the laser diode intensity is modulated via direct current modulation using an external RF signal generator, and the output electrical photoresponse of the µRTD-PD is measured from the RF port of the bias-T.

DBQW region, resulting in light-induced NDR regions (NDR 1–3 in Fig. 4a). Under forward bias, pronounced photoresponse is also observed, but only positive differential resistance is obtained. We relate this to the fact that under forward bias, there is insufficient band bending of the potential surrounding the DBQW region to obtain NDR effect. We have also measured the I–Vs under illumination with forward and downward voltage sweeps to verify hysteresis behaviour in our neuron (Supplementary S1), a property characteristic of memristor-based neurons. As shown in Fig. S1, our neuron devices do not exhibit hysteresis behaviour which enables stable bias conditions to operate our neuron devices for reliable neuromorphic applications.

To analyze the light-activated NDR in µRTD-PD devices of various dimensions we consider the effective optical power[39], $P_{\text{eff}} = P_{\text{in}}(A_{\text{pillar}}/A_{\text{spot}})$, launched into the micropillars where A_{pillar} is the active area of the micropillar, and A_{spot} is device light active area (uncovered surface of the pillar) corresponding to the illuminated area by the lensed fibre with a numerical aperture of 0.2. We have analysed the I–V curves under various optical excitation conditions, Fig. 4b. For P_{eff} ranging from 0.1 to 0.5 mW, we observe light-induced NDR regions (solid line in Fig. 4b at $P_{eff} = 0.2$ mW), however for $P_{eff} > 0.5$ mW the NDR signature is switched-off (dotted line in Fig. 4b). This indicates the NDR region in µRTD-PD devices can be switched-on for specific ranges of light intensity conditions. In the inset of Fig. 4b, the PVCR values of the NDR are presented as a function of P_{eff}. The PVCR increases gradually until reaching a maximum of PVCR = 1.11 at $P_{eff} = 0.25$ mW, and then decreases for

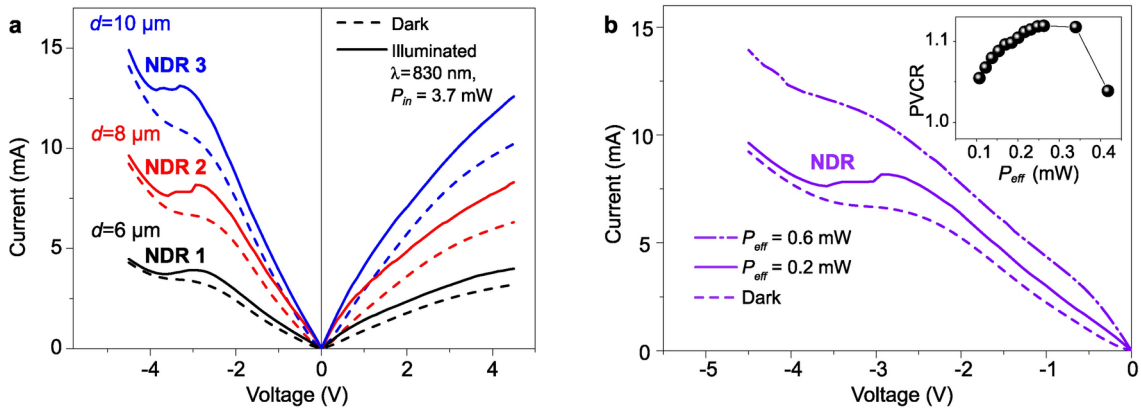

Fig. 4. Static characteristics of the μRTD-PD oscillatory neuron showing light-activation of the negative differential resistance region (NDR) and the evolution of the light-induced NDR and the peak to valley current ratio (PVCR) with effective input optical power. (**a**) Current–voltage (I-V) characteristics in reverse and forward bias voltage under dark (dashed-line) and near-infrared (NIR, $\lambda \sim 830$ nm) illumination (solid line) conditions for devices with $d = 6$ μm (NDR 1), $d = 8$ μm (NDR 2), and $d = 10$ μm (NDR 3). (**b**) Dark and illuminated I-V characteristics showing on and off switching of the NDR region with increasing effective input optical power P_{eff}. Inset is shown the PVCR as a function of P_{eff}. Here we selected a power range were the NDR region is clearly visible (in this case between 0.1 and 0.5 mW).

larger P_{eff}. Thus, given a sufficient large input power (here a threshold level of $P_{eff,th} > 0.5$ mW) the NDR is turned off (see Supplementary S2 and Fig. S2 for analysis of the neuron photoresponse).

Light-activation of oscillatory behaviour

To illustrate the working mechanism of our light-activated oscillatory neuron, our device is analysed considering the optoelectronic circuit of Fig. 1c, which emulates the FitzHugh–Nagumo oscillator model[40], a prototype of an excitable neuron system (see Supplementary, section S3). Under dark conditions, Fig. 5a, the I–V curve exhibits a smooth negative resistance region. As a result, there is not sufficient gain to sustain self-oscillations, and the neuron system tends to evolve to its steady-state value. This is illustrated by the small limit cycle (purple curve in panel (a)) and by the damped oscillations after initial conditions, panel (b). When illuminated, panel (c), and DC biased within the negative resistance region, sufficient gain is provided by the negative resistance and oscillatory behaviour can be sustained after initial conditions, panel (d), which is characterized by a stable limit cycle (purple line in panel c), i.e., a closed-orbit attractor in the current–voltage phase space.

In what follows, we present the results of generation of oscillatory behaviour when the NDR in the μRTD-PD sensory device is activated by CW NIR light. We employed an identical characterization setup described in the previous section (Fig. 3). Here, the μRTD-PD oscillatory response was measured through the RF port of the bias-T that was connected to an oscilloscope to characterize its oscillations in time domain (see Methods).

We focus our analysis on a μRTD-PD device with a diameter of $d = 6$ μm. Fig. 6a shows the evolution of the I–V characteristics under CW NIR illumination conditions ranging from $P_{in} = 6.8$ mW to $P_{in} = 14.3$ mW. To simplify the analysis in this section (and in the following sections), the input power parameter, P_{in}, is used instead of effective power, P_{eff}. When the region of NDR is light-activated, the device exhibits large-amplitude voltage self-sustained oscillations, Fig. 6b. The self-oscillations correspond to a limit cycle in the I–V phase space, Fig. 6. In Fig. 6b(i)–(iii) is shown the corresponding voltage oscillations ~ 350 kHz under increasing optical input power P_{in} collected from the 6 μm μRTD-PD using a reverse bias of $V_{DC} = -3.4$ V. The self-oscillation frequency is mainly determined by the equivalent circuit's resistance, R_s, equivalent circuit's inductance, L_s (which include the length of electrical metal contact pads, coaxial cables length and bias-T), μRTD-PD's intrinsic capacitance, C_{RTD}, and the nonlinear I–V characteristic negative resistance, $f(V, P_{in})$ (see in Fig. 1c the equivalent lumped-circuit). The self-oscillations observed here are lower than what is feasible with RTD-based devices whose quantum resonant tunnelling effect persists well beyond GHz[41]. Optimisation of the circuit, namely reducing coaxial lines parasitic inductance in the setup in combination with a circuit for stabilizing high-speed RF oscillations will enable higher speed oscillations[42]. The self-oscillation frequency of the circuit under CW illumination does not change substantially, showing only around 5% tunability (Fig. S5 in Supplementary). Significant changes are expected for devices designed for larger PVCR. Methods to increase the PVCR of our neuron device includes to modify the DBQW material composition or the relative barriers and well thicknesses.

Regarding amplitude of the oscillations, the magnitude of the amplitude is determined by the NDR voltage difference ($\Delta V = V_p - V_v$), and the difference between peak and valley current ($\Delta I = I_p - I_v$), which is controlled by the illumination conditions. In Fig. 6b(i)–(iii), the self-oscillations have lower amplitude under lower intensity illumination ($P_{in} = 6.8$ mW), mainly because of the low ΔI. The maximum power output of self-oscillations can be estimated as $P_{RFmax} = (3/16)(\Delta V \Delta I)$[43]. Therefore, as the illumination intensity increases, ΔI is higher, which leads to larger amplitude of self-oscillations. This monotonous trend is seen until the PVCR ratio increases. Assuming constant NIR illumination conditions, the self-oscillations can also be controlled by the bias voltage, V_{DC}. Panels (iv)–(vi) of Fig. 6b show the self-oscillation amplitude for three reverse bias conditions V_{DC} for a

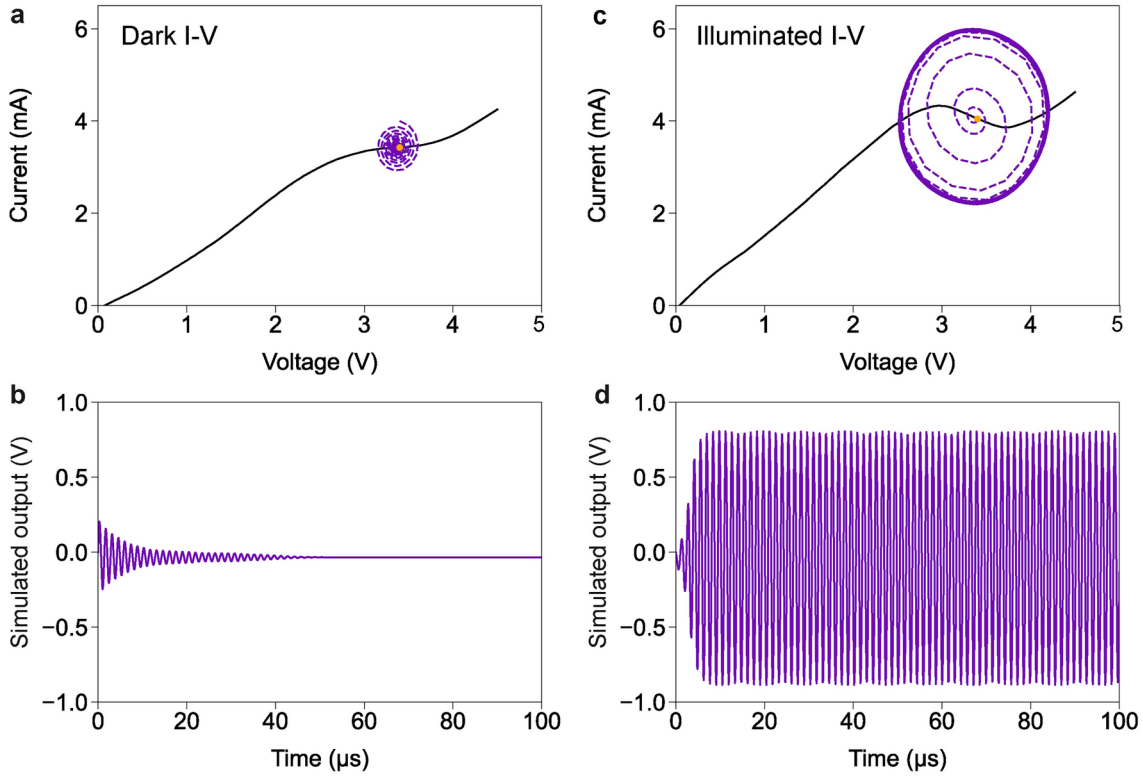

Fig. 5. Illustration of the oscillatory behaviour of the artificial neuron under dark and illumination conditions. (**a**) I–V fitting of the experimental dark I–V curve (black line) showing in the current–voltage phase space a small perturbation of the stable steady state due to initial conditions (purple line). (**b**) Simulated output voltage when the bias voltage is 3.4 V showing the system evolving to its steady-state value after initial conditions. (**c**) I–V fitting of the experimental illuminated I–V curve showing a large limit cycle (purple line) characterized by a closed-orbit attractor in the current–voltage phase space. (**d**) Simulated output voltage when the bias voltage is 3.4 V showing the system evolving to stable self-sustained oscillations.

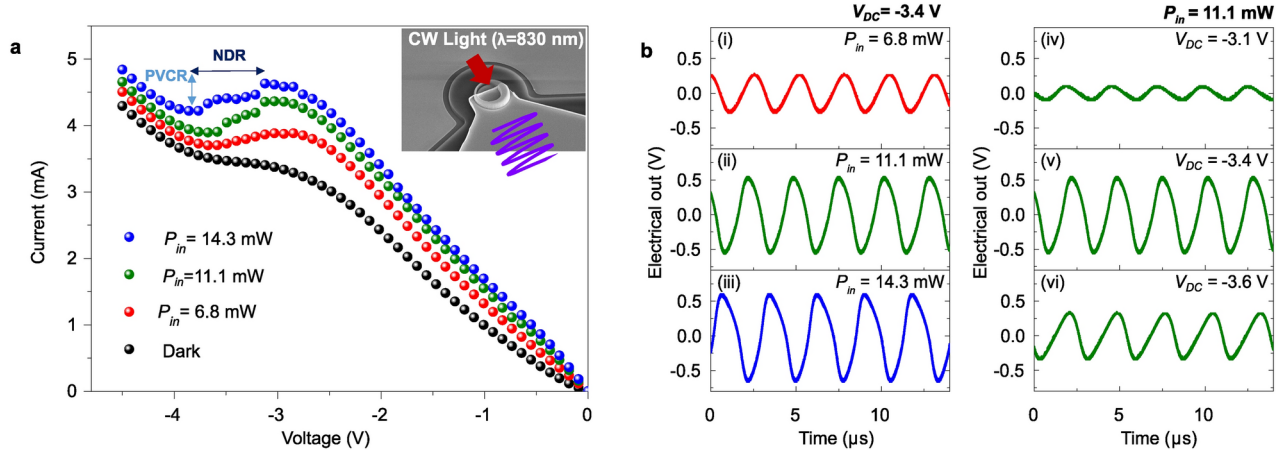

Fig. 6. Continuous-wave (CW) near-infrared (NIR, $\lambda = 830$ nm) illumination and activation of a region of negative differential resistance (NDR) and voltage oscillations. (**a**) Static I–V characteristics under dark (black dots) and illuminated (red, green and blue dots) conditions for $d = 6$ μm μRTD-PD under different illumination ($\lambda = 830$ nm) with optical power $P_{in} = 6.8$ mW, 11.1 mW and 14.3 mW. The inset shows a SEM image of a fabricated 6 μm sized μRTD-PD device exhibiting self-oscillation with illumination. (**b**) Left panel: self-sustained oscillations at a constant reverse bias voltage ($V_{DC} = -3.4$ V) and increasing illumination, (i) $P_{in} = 6.8$ mW, (ii) $P_{in} = 11.1$ mW, and (iii) $P_{in} = 14.3$ mW. Right panel: Self-sustained oscillations at a constant optical power $P_{in} = 11.1$ mW for increasing reverse bias (iv) $V_{DC} = -3.1$ V (close to the peak), (v) $V_{DC} = -3.4$ V (at the NDR centre), and (vi) $V_{DC} = -3.6$ V (close to the valley).

fixed illumination, P_{in} = 11.1 mW. The observed self-oscillation amplitude changes can be explained by the limit-cycle trajectory[30] taken by the oscillations in I–V phase space. Near the peak and valley voltage (V_p = − 3.1 V and V_v = −3.6 V, respectively), the amplitude (0.11 V and 0.33 V, respectively) is lower because of the smaller limit-cycle trajectory. The much lower amplitude at the peak voltage (V_{DC} = − 3.1 V) can be explained by the unstable periodic orbits of the limit cycle around the peak bias point[30]. When biased near the centre of the NDR region (V_{DC} = − 3.4 V), a larger limit cycle trajectory is obtained resulting in larger amplitude oscillations (0.56 V). Using the numerical model described in the Supplementary (Section S3), we have reproduced the experimental results of Fig. 6. Figures S2 and S3 show the simulations obtained for the self-oscillations under different illumination and bias voltage conditions, respectively, showing a good agreement with the experimental results.

Pulse-modulated light-induced excitatory and inhibitory oscillation response

In this section, we investigate the photo-induced excitatory and inhibitory control of the oscillation response in the µRTD-PD sensory neuron using pulse-modulated light, Fig. 7a. The goal is to demonstrate photo-switching between oscillatory and silent phase emulating dynamic neuronal-like signalling, a behaviour replicating visual-neuronal systems in nature[44]. In the experiment, the laser source was modulated by driving the laser current with electrical pulses with varying amplitude, V_{in}, at a frequency, f_{in}, ranging between 20 and 90 kHz. The light modulated frequencies are below the µRTD-PD circuitry self-oscillating frequency at around 350 kHz, as shown in Fig. 7b. The average intensity of the pulse-modulated light is defined as $<P_{in}>$.

Figure 7b, panels (i) and (ii), shows the all-or-nothing photo-switchable oscillatory behaviour of the µRTD-PD sensory device when reverse biased (V_{DC} = − 3.6 V, valley). In the case of illumination with a subthreshold average optical power (weak modulation, V_{in} = 20 mV, providing an average light intensity of $<P_{in}>$~3 mW) only self-sustained oscillations are observed, Fig. 7b(i), similarly as in the previous analysed case for CW illumination. However, for average pulse-modulation optical power above threshold (that is, with V_{in} = 40 mV providing $<P_{in}>$ ~ 4 mW), the µRTD-PD sensory neuron exhibits alternate periods of bursts of oscillations and silent response (without bursts), Fig. 7b(ii). This forms an inhibitory and excitatory oscillatory response which can be controlled by the optical power modulation frequency (f_{in}) and amplitude (V_{in}) of the incoming pulse-modulated light signals. This behaviour is analysed in more detail as follows.

First, we consider the photo-switchable response dependence on the amplitude using either positive or negative electrical pulses driving the laser source input. In a first case scenario, Fig. 7c(i), (ii), the µRTD-PD is biased near the valley region (V_{DC} = − 3.6 V) and perturbing positive pulses (increasing light intensity), panel (i), are injected in the µRTD-PD activating on/off firing of burst of oscillations. When the incoming pulse is at its baseline value (0 mV), the system remains biased in the NDR region forming the burst firing response. However, when the modulating pulse is at the high value (100 mV), the µRTD-PD neuron enters the 2nd positive differential resistance (PDC) region of the strong illuminated I–V curve (outside the NDR region), forming the silent response (without oscillations). In a second scenario, Fig. 7c (iii), (iv), the µRTD-PD is biased near the valley region (V_{DC} = − 3.6 V) and negative pulses (decreasing optical intensity), panel (iii), are injected in the µRTD-PD. In this case, when the pulse is in its baseline value (0 mV), the system remains biased in the NDR region forming the burst firing response. However, when the perturbing pulse is at its low value (-100 mV), the µRTD-PD neuron enters the PDC region of the dark I-V curve (with no NDR region), forming the silent response (without oscillations). We note the input pulse voltage in panels (i) and (iii) corresponds to the voltage RF input signal driving the laser current using direct modulation, which changes the average input optical power (experimental setup in Fig. 3). As a result, our artificial neuron is responding to increasing or decreasing of light intensity. As a result, the smaller amplitude of the burst firing responses in panel (iv) is attributed to lower average input optical power of $<P_{in}>$ = 2.5 mW as compared to panel (ii), $<P_{in}>$ = 6.8 mW. Therefore, by tuning the modulated light intensity of the incoming signals, excitatory and inhibitory oscillation responses can be controlled within the same µRTD-PD sensory neuron.

Lastly, Fig. 7d depicts the dynamics of the neuron-like burst oscillations as a function of the modulation frequency of the injected optical signal when the modulation amplitude is set constant (V_{in} = 40 mV). As observed in Fig. 7d(i)–(iii), the number of oscillation periods ("spikes") within each cycle can be fine-tuned. In this case the number of "self-oscillation periods" ("spikes") decreases as the frequency of modulation increases from (i) 20 kHz, and (ii) 40 kHz to (iii) 90 kHz. This enables an extra degree of freedom to encode incoming optical pulse information into oscillatory bursting signals.

Stability and spatiotemporal response of the burst oscillatory patterns

In this section, the stability and spatiotemporal response of the burst firing patterns are analysed. To this end, we use a space-time representation of the time-domain signals. In this representation, the position of a temporal pattern that repeats itself is clearly evidenced on a timescale much larger than the timescale of the oscillatory signals. This enables to analyse any drift (as for example induced by noise) of the experimental time traces. This space-time like diagram is commonly used for describing time-delayed systems[45].

Following a standard procedure, the recorded data is analysed in a spatially extended representation. The evolution of the burst firing patterns was recorded for a long time-period of about 0.2 s. The device was illuminated with pulse-modulated light (negative pulses, V_{in} = − 100 mV, f_{in} = 50 kHz) providing an average power output $<P_{in}>$~ 2.5 mW. In Fig. 8 is shown the space-time diagrams for various bias conditions across the NDR region of the µRTD-PD sensory neuron. The time within each cycle is plotted in the vertical axis and here we assume each cycle covers 60 µs (a total of 3333 cycles in the vertical axis). Here, the repetition rate of the incoming pulse-modulating signal is used as each round-trip (cycle). Near the peak, panel (a), a clear noise-induced drift motion of the oscillating patterns is observed. This indicates that noise in the system affects the stability of the burst oscillations. We attribute this to the higher current operation which contributes to electrical noise. The larger responsivity in the peak also contributes to shot noise. By selecting two representative cycles of

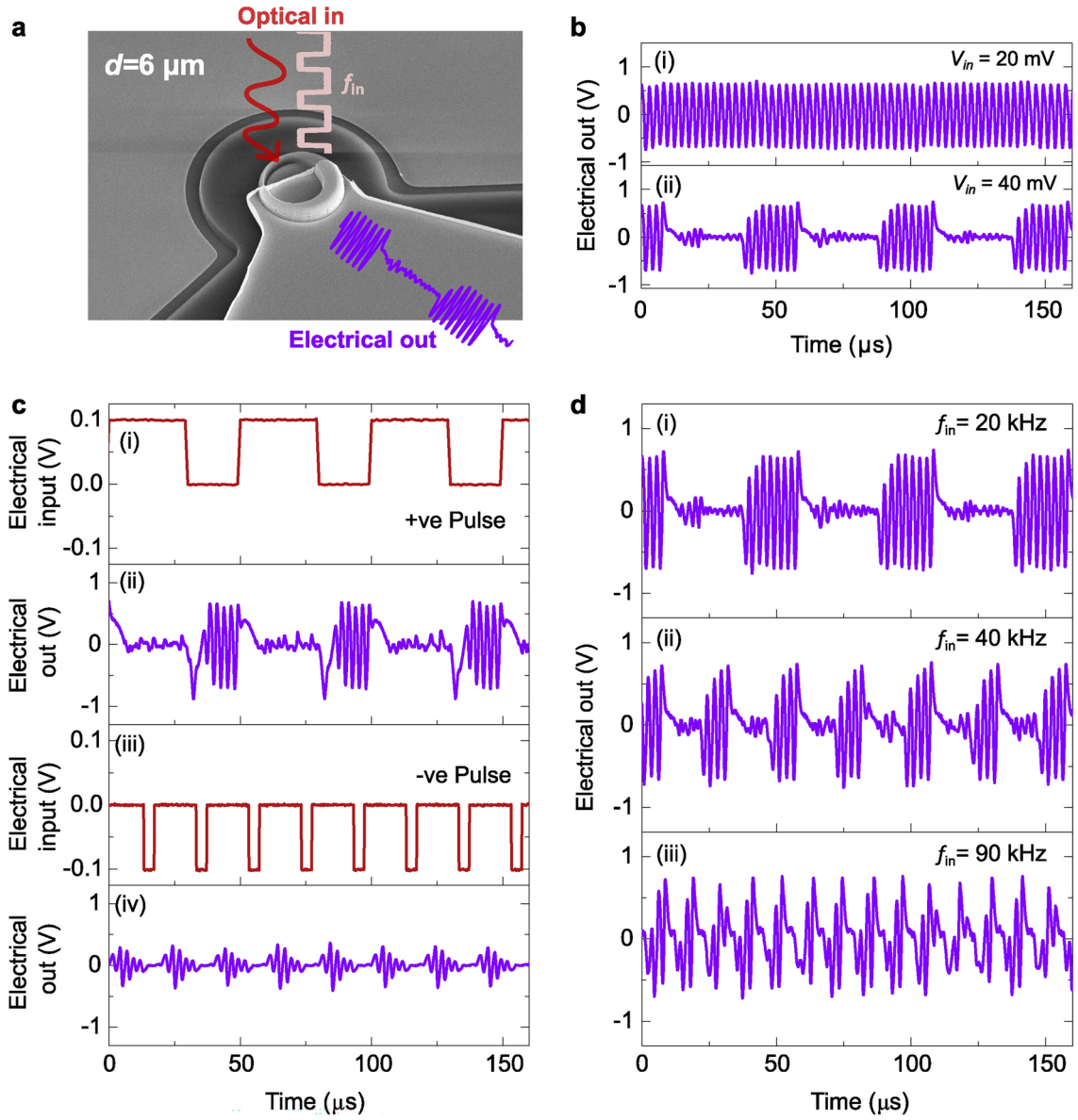

Fig. 7. Experimental oscillatory firing signalling activated by incoming pulse-modulated light. (**a**) Scanning electron microscope (SEM) picture of a single μRTD-PD oscillatory neuron device. For optical activation of the μRTD-PD neuron, pulse-modulated light at $\lambda \sim 830$ nm was used employing direct modulation of the laser with an electrical pulse signal with frequency, f_{in} and amplitude, V_{in}. (**b**) Electrical output showing neuron-like oscillatory signalling upon pulse-modulated light at frequency ($f_{in} = 20$ kHz) as a function of the amplitude (V_{in}): (i) self-sustained oscillations at $V_{in} = 20$ mV and $<P_{in}> \sim 4$ mW; (ii) oscillatory periodic firing activation at $V_{in} = 40$ mV and $<P_{in}> \sim 4$ mW. (**c**) Neuron-like oscillatory signalling responses using (ii) a positive pulse input [(i) $V_{in} = 100$ mV, $f_{in} = 20$ kHz, $<P_{in}> \sim 6.8$ mW], and (iv) a negative pulse input [(iii) $V_{in} = -100$ mV, $f_{in} = 50$ kHz, $<P_{in}> \sim 2.5$ mW]. (**d**) Burst firing activation using positive pulses ($V_{in} = 40$ mV and $<P_{in}> \sim 4$ mW) with variable frequency: (i) $f_{in} = 20$ kHz, (ii) $f_{in} = 40$ kHz, and (iii) $f_{in} = 90$ kHz.

the spatiotemporal map of Fig. 8a (panels (i) and (ii)), we can observe suppression of the burst oscillations (panel (ii)) within one cycle. This indicates that noise-induced drift motion contributes to supress burst oscillations. We note for the case of the patterns, panels (b) and (c), no suppression is observed for the time-period analysed here indicating stable patterns. The μRTD-PD oscillatory neuron spatiotemporal patterns are analogous to periodic breather-like oscillations observed in other neuron-like systems with slow-fast scales[44]. This behaviour has been reported in the context of neural activity in large neural networks, thus the μRTD-PD oscillatory neuron could be employed to study complex neuronal-like oscillatory spatiotemporal patterns in brain circuits.

Finally, since endurance is one important characteristics of neuron devices for reliable neuromorphic applications, in Fig. 9 we evaluate the stability and reliability of generated spike trains in response to the input. This was done by evaluating the spike trains on-off peak amplitude in response to a fixed input for a long acquisition time (>10^3 cycles, only limited by the oscilloscope acquisition time) and changing the DC bias point

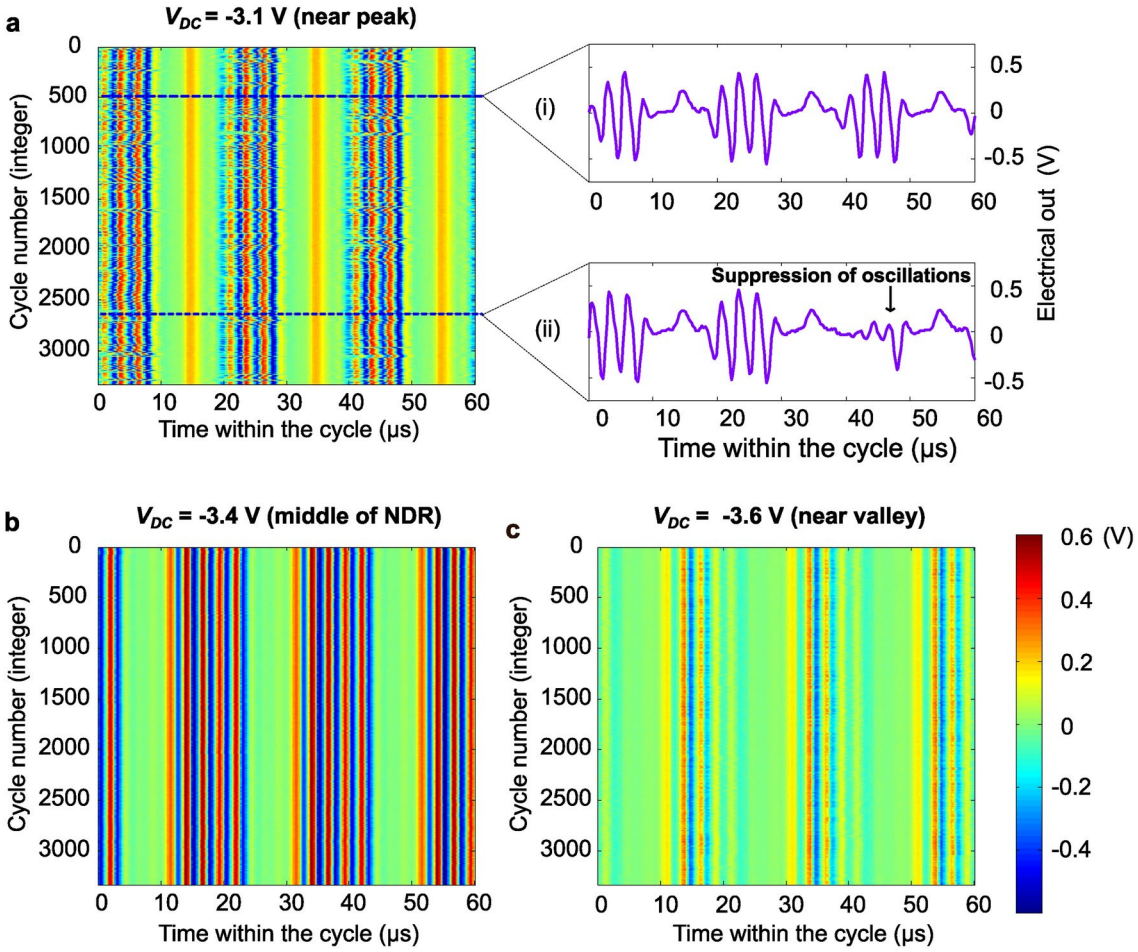

Fig. 8. Spatiotemporal plots showing the evolution of the burst firing oscillations over a 0.2 s time-period. In this co-moving reference frame, the horizontal axis is a space-like coordinate that allows to localize the position of the burst oscillations within a given cycle while the vertical axis corresponds to the slow temporal evolution of the system over various cycles. (**a**) Space–time plot of burst firing oscillations when the μRTD-PD neuron is biased near the peak voltage, $V_{DC} = -3.1$ V. The insets (i) and (ii) represent the time traces at cycle 500 and 2600, respectively, showing suppression of oscillations in panel (ii). Space–time plot of burst firing oscillations when the μRTD-PD neuron is biased in: (**b**) the middle of the NDR region, $V_{DC} = -3.4$ V, and (**c**) in the near-valley region, $V_{DC} = -3.6$ V. All the measurements use the same contour plot scale denoting the amplitude of the μRTD-PD output, depicted on the right side of panel (**c**).

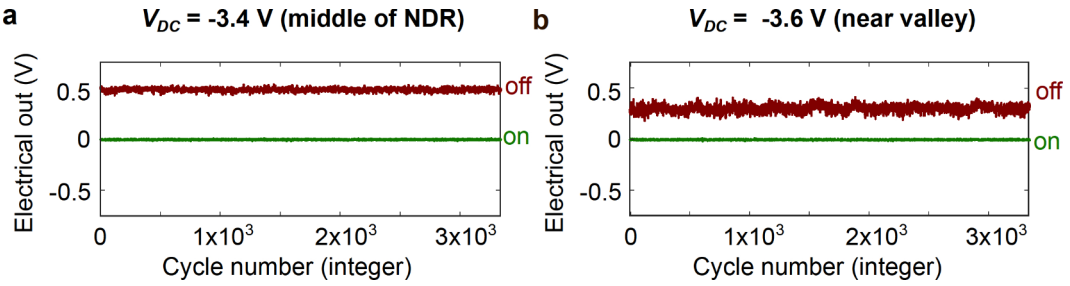

Fig. 9. Experimental results which evaluate the spike trains on–off peak amplitude in response to a fixed input for a long acquisition time ($> 10^3$ cycles) in (**a**) middle of the NDR region and (**b**) near the valley region.

	Material platform	Wavelength (nm)	Monolithic integrated photodetector and neuron	Energy/event (J)	Pulse/spike event timescales	Neuron functions
Phase change materials[47]	GeSbTe/Si	1550	No	$\sim 10^{-12}$	500 ps–1.5 ns (read and write)	Integrate-and-fire
Izhikevich photonic neuron[48]	CMOS with Si photonics	1550	No	$\sim 10^{-12}$	~1 ns	Regular and fast spiking/chattering
Photodetector-memristor hybrid systems[24]	Hybrid Ta/IGZO4/Pt with Ta/NbO_x/Pt	254–365	No	–	< 1 µs	Oscillatory
Memristor systems[49]	Pt/Co_3O_{4-x}/ITO	–	No	–	< 1 s	Oscillatory/bursting
Transistor neuron[50]	CMOS	1550	No	$\sim 10^{-9}$	~ 1 s	Integrate-and-fire
This work	III–V: GaAs	830	Yes	$\sim 10^{-12}$	~ 1 µs	Oscillatory/spike bursting

Table 1. Optically activated oscillator and spike-based neurons in various material platforms including photonics, electronics and hybrid electronic-photonic.

within the NDR region (panels a and b). The results suggest that the most stable operation is when the device is DC biased in the middle of the NDR. In this case, a clear on-off of the oscillations with small fluctuation of the spike amplitude is observed, panel a), while near the valley the spike train shows fluctuations of its peak amplitude, panel b). As a conclusion, for robust operation of the neuron as a spike train emitter, operation in the middle of the NDR provides the most reliable performance.

Discussion

We demonstrated a III–V neuromorphic photonic oscillator neuron consisting of a micropillar quantum resonant tunnelling diode (RTD) with GaAs photosensitive absorption layers, the µRTD-PD sensory oscillator neuron. The µRTD-PD sensory device responds to incoming analogue optical signals, enabling light-activation of negative differential resistance (NDR) of relevance to emulate FitzHugh–Nagumo-type of neuron models. We fabricated µRTD-PD devices of various diameters (d = 6 µm, 8 µm and 10 µm), and investigated the static I-V characteristics under dark and near-infrared light conditions. A noticeable increase of the photocurrent was observed in the so-called peak voltage in reverse bias conditions, resulting in a significant increase of the devices' optical responsivity and subsequent light-induced NDR region.

In this work, we focused on the analysis of bursting oscillatory patterns, a behaviour highly relevant in visual sensory neuronal biological systems. Taking advantage of the NDR effect, we demonstrated µRTD-PD functioning as sensory oscillatory neurons where oscillations can be activated using low intensity optical power. Using pulse-modulated light, excitatory and inhibitory control of spatiotemporal neural-like oscillations was demonstrated, emulating oscillatory and silent phase dynamic neuronal signalling and simulating neural activity in networks in the form of breather-type oscillatory phenomena.

The light-induced NDR and oscillatory phenomena were observed at an effective power as low as $P_{eff} \sim 100$ µW. Considering the estimated lensed fibre coupling efficiency ($\eta_c \sim 8 \times 10^{-4}$) in the experiments[39], and assuming a pulse frequency of the incoming pulse of 350 kHz (as fast as the self-oscillations), we obtain an optical pulse activation energy of ~ 230 fJ per burst oscillations, where the energy is calculated as $E = \eta_c P_{eff}/f_{in}$. Improvements include optimization of the light absorption in the micropillars as for example using nanostructuring of the micropillar. Also, optimization of speed operation could further reduce the optical energy requirements to activate optically the neuronal oscillatory functions. We note µRTD-PD devices have higher-speed oscillatory potential, since quantum resonant tunnelling effect in RTD-based devices persist well beyond GHz. Higher frequency operation is achievable via optimisation of the circuit, namely through the reduction of parasitic inductance from the experimental setup.

In Table 1, we provide a benchmark of recent examples of optically activated oscillator and spike-based neurons in various material platforms. Our neuron emulates the physiology of neurons and their oscillatory dynamics which goes beyond the simple leak-integrated-and-fire functions implemented in photonics[46] and complementary metal–oxide–semiconductor (CMOS)[47] approaches. Compared with electronics and electronic-photonics[24,48,49], our approach enables monolithic integration of the photodetector and neuron within a single device, without additional circuitry which increases the power consumption and footprint of the neuron hardware. As a result, this provides potential for scalability since miniaturization from micropillar to nanopillar[38] neurons could enable larger number of neurons in a single chip. Importantly, our neuron uses identical III–V materials that have matured to meet the demanding industrial requirements of 3D sensing and LiDAR systems. Lastly, regarding integrability, we have shown recently that a similar semiconductor architecture exhibits negative resistance and electroluminescence[39], providing the possibility for artificial neuron emitters. This combined with interconnected links[50], could enable emitter-receiver neurons for in-sensor neuromorphic edge computing applications.

Methods

Epilayer design

The epilayer stack of the n–i–n type (Si-doped) GaAs µRTD-PD oscillatory neuron was grown by metal organic chemical vapour deposition (MOCVD) on a semi-insulating (SI) GaAs substrate. In Fig. 1b is depicted the schematic of the µRTD-PD semiconductor epilayer stack, including the double barrier quantum well (DBQW)

intrinsic region. The DBQW is formed by a stack of AlAs/GaAs/AlAs (1.4 nm/7 nm/1.4 nm) layers, surrounded by a GaAs layer of 5 nm forming the emitter and collector spacer layers, all of which are unintentional doped. Surrounding the intrinsic region with DBQW we have lightly doped *n*-GaAs ($N_d = 2 \times 10^{16}$ cm^{-3}) photoabsorption layers with 300 nm and 500 nm thicknesses on the emitter and collector sides respectively (in the scenario of forward bias operation). The emitter cladding layer (which is also the bottom contact layer) consist of a 300 nm thick graded $Al_xGa_{1-x}As$ layer (where x varies from 0 to > 0.3) moderately doped with $N_d = 2 \times 10^{18}$ cm^{-3}. The collector cladding consists of a 300 nm thick $Al_{0.3}Ga_{0.7}As$ layer with a moderate *n*-type doping concentration ($N_d = 2 \times 10^{18}$ cm^{-3}). The collector top contact is formed by a highly doped 150 nm thick *n*-GaAs ($N_d = 5 \times 10^{18}$ cm^{-3}).

Fabrication

The MOCVD grown 6-inch wafer is first diced into 1 inch square samples. The μRTD-PD devices were fabricated by defining micropillars by optical lithography by using direct laser writing, followed by etching using induced couple plasma reactive ion etching (ICP-RIE) until reaching the bottom *n*-contact $Al_xGa_{1-x}As$ layer (etch depth of ~ 1.3 μm). The micropillars were then passivated with a thick layer (~ 1 μm) of SiO_2, and via openings for the bottom and top contacts were defined by optical lithography, followed by dry etching of the SiO_2. Both the top and bottom metal contacts (using a coplanar waveguide transmission line design) were formed using Ge/Ni/Au (20 nm/10 nm/150 nm) metal alloys. Finally, samples of fabricated devices were subjected to rapid thermal annealing at 400 °C for 30 s.

Optoelectronic characterization

The μRTD-PDs were electrically connected using a ground-signal-ground (G-S-G) coplanar waveguide electrical probe connected to a bias-T (bandwidth of 0.1–4200 MHz). The photodetection setup consists of lensed fibre coupled to a pigtail continuous wave (CW) laser diode source in a single-mode fibre, $\lambda = 830 \pm 10$ nm (Roithner Lasertechnik, model SPL830-5-4-PD), where the respective photocurrent was monitored via the DC port of the bias-T by the change in the I–V characteristics obtained from Keithley 2280S DC source meter upon optical injection of the μRTD-PD. The intensity from the laser diode was controlled by a current driver and temperature controller (Thorlabs, CLD1010LD) and the modulation was provided by an electrical signal generator (RIGOL, model DG1000Z). The input optical powers were calibrated by a commercial power meter (Newport, model 1918-R). The laser diode was electrically pumped to obtain an average optical power $<P_{in}>$. The pulse-modulated laser intensity was fed into the μRTD-PD top pillar and the electrical RF output was collected using an oscilloscope (R&S, MXO oscilloscope) which was connected to the AC port of the bias-T.

Data availability

The data supporting this study's results is available from the corresponding author on reasonable request.

Received: 23 February 2024; Accepted: 11 February 2025
Published online: 25 February 2025

References

1. Roy, K., Jaiswal, A. & Panda, P. Towards spike-based machine intelligence with neuromorphic computing. *Nature* **575**, 607 (2019).
2. Sebastian, A., Le Gallo, M., Khaddam-Aljameh, R. & Eleftheriou, E. Memory devices and applications for in-memory computing. *Nat. Nanotechnol.* **15**, 529–544 (2020).
3. Sharf, T. et al. Functional neuronal circuitry and oscillatory dynamics in human brain organoids. *Nat. Commun.* **13**, 1–20 (2022).
4. Akopyan, F. et al. TrueNorth: Design and tool flow of a 65 mW 1 million neuron programmable neurosynaptic chip. *IEEE Trans. Comput. Des. Integr. Circuits Syst.* **34**, 1537–1557 (2015).
5. Neuromorphic Computing and Engineering with AI|Intel®. https://www.intel.com/content/www/us/en/research/neuromorphic-computing.html.
6. On, M. B., Xiao, X., Proietti, R., Lee, Y.-J. & Yoo, S. J. B. Photonic spiking neural networks with event-driven femtojoule optoelectronic neurons based on Izhikevich-inspired model. *Opt. Express* **30**, 19360–19389 (2022).
7. Buzsáki, G. Rhythms of the Brain. *Brain* **1**, 1–464 (2006).
8. Tang, M. et al. An extra-clock ultradian brain oscillator sustains circadian timekeeping. *Sci. Adv.* **8**, 5506 (2022).
9. Fabian, J. M. & Wiederman, S. D. Spike bursting in a dragonfly target-detecting neuron. *Sci. Rep.* **11**, 1–6 (2021).
10. Ferres, E. et al. Large-scale, high-resolution electrophysiological imaging of field potentials in brain slices with microelectronic multielectrode arrays. *Front. Neural Circuits* **6**, 1–14 (2012).
11. Menzler, J. & Zeck, G. Network oscillations in rod-degenerated mouse retinas. *J. Neurosci. Off. J. Soc. Neurosci.* **31**, 2280–2291 (2011).
12. Ito, J. et al. Whisker barrel cortex delta oscillations and gamma power in the awake mouse are linked to respiration. *Nat. Commun.* **5**, 3572 (2014).
13. Song, K. M. et al. Skyrmion-based artificial synapses for neuromorphic computing. *Nat. Electron.* **3**, 148–155 (2020).
14. Zhang, X. et al. An artificial spiking afferent nerve based on Mott memristors for neurorobotics. *Nat. Commun.* **11**, 1–9 (2020).
15. Wu, Z. et al. A habituation sensory nervous system with memristors. *Adv. Mater.* **32**, 2004398 (2020).
16. Zhang, S. et al. Selective release of different neurotransmitters emulated by a p–i–n junction synaptic transistor for environment-responsive action control. *Adv. Mater.* **33**, 2007350 (2021).
17. Pickett, M. D., Medeiros-Ribeiro, G. & Williams, R. S. A scalable neuristor built with Mott memristors. *Nat. Mater.* **12**, 114–117 (2012).
18. Wan, C. et al. An artificial sensory neuron with visual-haptic fusion. *Nat. Commun.* **11**, 1–9 (2020).
19. Tan, H. et al. Tactile sensory coding and learning with bio-inspired optoelectronic spiking afferent nerves. *Nat. Commun.* **11**, 1–9 (2020).
20. Tuma, T., Pantazi, A., Le Gallo, M., Sebastian, A. & Eleftheriou, E. Stochastic phase-change neurons. *Nat. Nanotechnol.* **11**, 693–699 (2016).
21. Kim, Y. et al. A bioinspired flexible organic artificial afferent nerve. *Science* **360**, 998–1003 (2018).
22. Yoon, J. H. et al. An artificial nociceptor based on a diffusive memristor. *Nat. Commun.* **9**, 1–9 (2018).
23. Seo, S. et al. Artificial optic-neural synapse for colored and color-mixed pattern recognition. *Nat. Commun.* **9**, 1–8 (2018).

24. Wu, Q. et al. Spike encoding with optic sensory neurons enable a pulse coupled neural network for ultraviolet image segmentation. *Nano Lett.* **20**, 8015–8023 (2020).
25. Romeira, B. et al. Brain-inspired nanophotonic spike computing: challenges and prospects. *Neuromorphic Comput. Eng.* **3**, 033001 (2023).
26. Peng, H. T. et al. Neuromorphic photonic integrated circuits. *IEEE J. Sel. Top. Quant. Electron.* **24**, 1–15 (2018).
27. Robertson, J., Hejda, M., Bueno, J. & Hurtado, A. Ultrafast optical integration and pattern classification for neuromorphic photonics based on spiking VCSEL neurons. *Sci. Rep.* **10**, 6098 (2020).
28. Shastri, B. J. et al. Photonics for artificial intelligence and neuromorphic computing. *Nat. Photon.* **15**, 102–114 (2021).
29. Winge, D. O. et al. Implementing an insect brain computational circuit using III–V nanowire components in a single shared waveguide optical network. *ACS Photon.* **7**, 2787–2798 (2020).
30. Ortega-Piwonka, I., Piro, O., Figueiredo, J., Romeira, B. & Javaloyes, J. Bursting and excitability in neuromorphic resonant tunneling diodes. *Phys. Rev. Appl.* **15**, 034017 (2021).
31. Rocşoreanu, C., Georgescu, A. & Giurgiţeanu, N. *The FitzHugh-Nagumo Model* Vol. 10 (Springer, 2000).
32. Romeira, B., Avo, R., Figueiredo, J. M. L., Barland, S. & Javaloyes, J. Regenerative memory in time-delayed neuromorphic photonic resonators. *Sci. Rep.* **6**, 1–12 (2016).
33. Romeira, B., Figueiredo, J. M. L. & Javaloyes, J. Delay dynamics of neuromorphic optoelectronic nanoscale resonators: Perspectives and applications. *Chaos An Interdiscip. J. Nonlinear Sci.* **27**, 114323 (2017).
34. Raghib, Q. et al. Optically-triggered deterministic spiking regimes in nanostructure resonant tunnelling diode-photodetectors. *Neuromorphic Comput. Eng.* **3**, 034012 (2023).
35. Buzsáki, G. & Draguhn, A. Neuronal olscillations in cortical networks. *Science* **304**, 1926–1929 (2004).
36. Ironside, C., Romeira, B. & Figueiredo, J. *Resonant Tunnelling Diode Photonics Devices and Applications* 2nd edn. (IOP Publishing, 2023).
37. Brown, E. R., Zhang, W. D., Growden, T. A., Fakhimi, P., & Berger, P. R. (2021). Electroluminescence in unipolar-doped In0.53Ga0.47As/AlAs resonant-tunneling diodes: A competition between interband tunneling and impact ionization. *Phys. Rev. Appl.* **16** (2021).
38. Jacob, B. et al. Surface passivation of III–V GaAs nanopillars by low-frequency plasma deposition of silicon nitride for active nanophotonic devices. *ACS Appl. Electron. Mater.* **4**, 3399–3410 (2022).
39. Jacob, B. et al. Room-temperature electroluminescence and light detection from III–V unipolar microLEDs without p-type doping. *Optica* **10**, 528 (2023).
40. Izhikevich, E. M. Neural excitability, spiking and bursting. *Int. J. Bifurc. Chaos* **10**, 1171–1266 (2000).
41. Maekawa, T., Kanaya, H., Suzuki, S. & Asada, M. Oscillation up to 1.92 THz in resonant tunneling diode by reduced conduction loss. *Appl. Phys. Express* **9**, 024101 (2016).
42. Wang, L., Figueiredo, J. M. L., Ironside, C. N. & Wasige, E. DC characterization of tunnel diodes under stable non-oscillatory circuit conditions. *IEEE Trans. Electron Devices* **58**, 343–347 (2011).
43. Cimbri, D., Wang, J., Al-Khalidi, A. & Wasige, E. Resonant tunneling diodes high-speed terahertz wireless communications: A review. *IEEE Trans. Terahertz Sci. Technol.* **12**, 226–244 (2022).
44. Chouzouris, T. et al. Chimera states in brain networks: Empirical neural vs modular fractal connectivity. *Chaos* **28**, 1–10 (2018).
45. Romeira, B. et al. Broadband chaotic signals and breather oscillations in an optoelectronic oscillator incorporating a microwave photonic filter. *J. Light. Technol.* **32**, 3933–3942 (2014).
46. Feldmann, J., Youngblood, N., Wright, C. D., Bhaskaran, H. & Pernice, W. H. P. All-optical spiking neurosynaptic networks with self-learning capabilities. *Nature* **569**, 208–214 (2019).
47. Han, J.-K. et al. Bioinspired photoresponsive single transistor neuron for a neuromorphic visual system. *Nano Lett.* **20**, 8781–8788 (2020).
48. Lee, Y.-J. et al. Demonstration of programmable brain-inspired optoelectronic neuron in photonic spiking neural network with neural heterogeneity. *J. Light. Technol.* **42**, 4542–4552 (2024).
49. Liu, H. et al. Artificial spiking neuron with bursting dynamics for noise-resistant neuromorphic coding. *ACS Appl. Electron. Mater.* **5**, 3454–3461 (2023).
50. Adão, R. M. R., Alves, T. L., Maibohm, C., Romeira, B. & Nieder, J. B. Two-photon polymerization simulation and fabrication of 3D microprinted suspended waveguides for on-chip optical interconnects. *Opt. Express* **30**, 9623–9642 (2022).

Acknowledgements

We acknowledge the financial support by European Union, H2020-FET-OPEN framework programme, Project 828841—ChipAI, Horizon Europe, project 101046790—InsectNeuroNano, and Fundação para a Ciência e a Tecnologia (FCT) project 2022.03392.PTDC—META-LED. We acknowledge access and support by the Micro and Nanofabrication Facility (especially Joana Santos and José Fernandes) and the Nanophotonics and Bioimaging Facility at INL. We also acknowledge Qusay Raghib Ali Al-Taai, Jue Wang, and Edward Wasige of the University of Glasgow for the annealing of samples, and the discussions of the design of the coplanar waveguide transmission line-based electrical contacts. We acknowledge the fruitful discussions with Antonio Hurtado regarding optically driven neuron-like behaviour in RTD photodetector devices. BJ acknowledges the support in frame of the PhD program in Electrical Engineering, Electronics and Automation at Carlos III University of Madrid, Department of Electronic Technology, Group of Displays and Photonic Applications, Avda de la Universidad, 30, 28911, Leganes, Madrid, Spain.

Author contributions

B.R. and J.M.L.F. contributed to the design of the devices. J.M.L.F. contributed to the design of the III–V epilayer stack. B.J. fabricated and characterized the devices. B.J., J.B.N. and B.R. conceived the experiments. J.S. implemented the simulation numerical results of a model of the experimental artificial neuron. All authors contributed to the analysis and interpretation of the results. B.J and B.R. wrote the manuscript. All authors reviewed the manuscript.

Declarations

Competing interests

The authors declare no competing interests.

Additional information

Supplementary Information The online version contains supplementary material available at https://doi.org/10.1038/s41598-025-90265-z.

Correspondence and requests for materials should be addressed to B.J. or B.R.

Reprints and permissions information is available at www.nature.com/reprints.

Publisher's note Springer Nature remains neutral with regard to jurisdictional claims in published maps and institutional affiliations.